Asian Journal of Chemistry; Vol. 34, No. 9 (2022), 2257-2264

ASIAN JOURNAL OF CHEMISTRY

https://doi.org/10.14233/ajchem.2022.23879

Facile Fabrication of Manganese Dioxide Composite Incorporated Aluminium Rich Alloy Metal Matrix as Efficient Sacrificial Anodes

K.K. BINOJ* and P.Y. JINU

Department of Chemistry, Catholicate College (Affiliated to Mahatma Gandhi University), Pathanamthita-689645, India

*Corresponding author: E-mail: kbinuk82@gmail.com

Received: 23 April 2022; *Accepted*: 17 May 2022; *Published online*: 19 August 2022; AJC-20919

Nanosized manganese dioxide was prepared by anodic electro deposition method under standardized experimental conditions. Aluminum-zinc alloy sacrificial anodes incorporated with MnO_2 nanoparticles were fabricated for cathodic protection of steel. The physico-chemical properties of anodes were enhanced by uniform dispersion and infiltration of the nano-MnO_2 particles into the Al-Zn matrix. Such effective and uniform presence of nano-MnO_2 inside the interior mass of the anodes was characterized by electrochemical techniques. The anodes exhibited stable potential in open circuit, small polarization and significant rate of depletion in self-corrosion in the course of galvanic immersion studies. The existence of nanocomposite particles in the anode matrix caused effective destruction of the passive aluminia film, which facilitated enrichment of galvanic performance of anode. The anode had better endurance against biofouling also.

Keywords: Aluminium alloy, Metal matrix composites, Corrosion, Nanoconposites.

INTRODUCTION

Aluminum is one of the most effective and economical substrate for cathodic protection of steel due to its high current capacity, low density, inherent negative potential and reasonable cost [1-3]. However, pure Al supports nano range protective oxide film, which knock out it as impractical in marine conditions. The alloying elements like Ga, Ce, Hg, La, Se and Zn shifts open circuit potential (OCP) from –1.18 to –1.10 V *versus* saturated calomel electrode (SCE), an operating potential from –1.12 to –1.05 V *versus* SCE, a current efficiency of more than 85%, and an anode capacity of more than 2600 h Kg^{-1} [4-8], causing so-called activation of Al alloy sacrificial anode. Most of the works in the field were carried out on Al-rich Zn sacrificial anode where Zn destabilize the Al_2O_3 layer due to the formation of $ZnAl_2O_4$ spinel, and the concentration of Zn has been optimized to 5 wt.% due to enhancement in physico-chemical and galvanic characteristics by forming of β-phase [9]. Hence, the aluminium-zinc alloys were considered for this study as well.

The increased demand from industries for aluminium sacrificial anode having better galvanic and metallurgical performance has initiated the search for new aluminium metal matrix composites (MMCs) anode. Recent developments in this field were the incorporation of solid ceramic composites particles into the metal matrix. Discontinuously reinforced aluminum metal matrix composites exhibits blending properties of both composites and matrix led to significant enhancement in the physico-chemical and galvanic properties [10]. The incorporation of metal composites can also modifies boundaries of grains, preventing deterioration along the grain boundaries. The inclusion of CeO_2, SiO_2, ZrO_2 and TiO_2 in the Al matrix can effectively suppress the non-columbic metal loss leading to considerable improvement in galvanic characteristics [11-13].

Recently, it was reported that the incorporation of composites in Al-Zn alloy sacrificial anode cause local thinning of passive Al_2O_3 layer which in-turn activate the sacrificial anode [14]. Within the category of metal oxides, manganese dioxide based systems are presently receiving considerable attention from the scientific community [15]. The popularity of MnO_2 can be attributed to its unique combination of physico-chemical and electrochemical properties, such as a relatively high density and purity and the spectrum of possible discharge rates maintainable for prolonged periods of time [16,17]. The wide range of technological applications of manganese dioxide includes catalysis, ion exchange, molecular adsorption, biosensors and

particularly in energy storages [18-21]. Microsized MnO_2 inclusion into aluminium substantially enhances physico-chemical and metallurgical properties [22]. Incorporation of MnO_2 could also led to considerable enhancement in mechanical and structural features of the alloy [23,24]. The present study design to investigate and valuates the activator characteristics of nano MnO_2 for the effective sacrificial dissolution of Al-Zn anode.

EXPERIMENTAL

Synthesis of nano MnO_2: Nanosized manganese dioxide was prepared by anodic electrodeposition method [25]. The cell used for electrodeposition was based on a temperature controlled 2 L glass beaker in which two titanium sheets (25 cm^2) were used as the anode substrate, and three similarly sized copper sheets were used as the cathode substrate. The electrodes were arranged alternately so that each anode was surrounded on both sides by a cathode. The electrolyte was an aqueous mixture ranging from 0.05 to 0.5 M $MnSO_4$ and 0.01 to 1.0 M H_2SO_4 maintained at an elevated temperature (90-99 ºC). Electrodeposition of MnO_2 was conducted with an anodic current density within the range 10-100 A m^{-2}. The overall process was carried out for three days, during that time the electrolyte Mn^{2+} concentration was of course depleted, while H^+ concentration increased. To counteract this, and hence maintain a constant electrolyte composition over the duration of the deposition, a concentrated (1.5 M) $MnSO_4$ solution was added continually at a suitable rate to replenish Mn^{2+} and dilute any excess H_2SO_4 added. After the deposition was complete, the solid manganese dioxide deposit was mechanically removed from the anode.

Characterization of nano MnO_2: The particle size characterization was carried out by X-ray diffraction analysis (Philips X′ Pert MPD X-ray powder diffractometer using Cu$K\alpha$ (λ = 1.540 Å) and was further confirmed by TEM using 2000 Fx-11, Transition Electron Microscope, JEOL, Japan. HR-TEM micrographs were obtained with a Hitachi Hf-2000 FE-TEM instrument equipped with a Kevex energy dispersive X-ray detector operated at 200 kV. Particle size analyzer Shimadzu SALD-2300 was used for particle size profile.

Anode molding: Commercial grade Al (99.75 %) and Zn (99.05 %) rods were explored to molding Al -Zn sacrificial anode. This combination of Al and Zn forms a homogeneous solid solution with uniform grain size and grain boundaries throughout the entire crystal lattice. The alloy ingots were cut, weighed and melted in a graphite crucible, kept in muffle furnace at 710 ± 10 ºC. Different amounts of nano MnO_2 particles were added into the melt and stirred using a SiC rod to homogenize it. The melt was again kept in muffle furnace for 15 min at the same temperature and then poured in to a preheated graphite die of dimension 5.5 cm × 3.5 cm × 0.5 cm.

Microstructural evaluation: Metallurgical characterizations of the anodes were carried out using Hitachi S- 2400 scanning electron instrument. The samples were cut from the center of the bulk of the fabricated sacrificial anode surface. They were clearly well ground and serially polished up to 600 grits using SiC paper and then mirror polished sequentially with 0.1 µm and 0.05 µm Al_2O_3 slurry.

Electrochemical evaluation

Decay of OCP: A fixed area of the anode was exposed in electrolyte and a copper wire was connected to make electrical contact. The electrode-electrolyte interface can be studied in terms fluctuations in OCP shift for a time period of 60 days. All the samples were dipped in a medium of 3% NaCl solution at temperature of 30 ± 2 ºC. The change in OCP and CCP was measured at regular intervals of every minute initially and then after every 24 h till 60 days.

Weight loss measurement: The difference in the weight of the coupons before and after immersion was measured after cleaning the anodes using a standard procedure (ASTM G 31). The rate of self corrosion was evaluated based on the weight loss measurement data.

Efficiency of anode: The casted anode and a large steel cathode having exposed surface area 1:10 was connected with insulated copper wire. All the anode-cathode samples were dipped simulated sea water and monitored the current moving across the anode-cathode couple. The reduction in anode weight before and after the experimental periods was determined according to ASTM G 31. The theoretical galvanic capacity of the casted anode was calculated from the data of reduction in anode weight.

Electrochemical impedance characterization: Electrochemical impedance spectroscopy (EIS) was studied with electrochemical analyzer (Auto lab PG stat 30 plus FRA 2). Ag/AgCl, Pt and the anode having 1 cm^2 exposed area were as reference, counter and working electrodes, respectively. The electrolyte used was 3% NaCl. The impedance studies were done at 1 MHz to 0.1 Hz with reference to OCP after 30 min exposure of the anodes in the electrolyte.

Biogrowth: The total number of viable counts (TVC) was calculated by standard procedure of plate counting techniques. The surface biofilm formed on the given anode surface was mixed with peptone water. This mixtures was shaken for 5 min so that all micro organisms were serially diluted with sterile water to get 10-5 dilution. Then, 1mL of mixture was spotted on to the Zobell marine agar medium. The temperature and pH were 25 ºC and 7.6 ± 0.2, respectively and a time period of 24-48 h were taken for the incubation of the plates. From this the colony forming unit (CFU) was calculated.

RESULTS AND DISCUSSION

Characterization of nano MnO_2: Fig. 1a shows X-ray diffraction (XRD) pattern of the MnO_2 sample. The pattern is similar to that of a typical commercial electrolytic MnO_2 (EMD) and the γ-MnO_2 reported in the literature [26,27]. The diffraction peaks occurred at 21.88º, 37.16º, 42.50º, 55.96º and 67.30º, respectively should be assigned to the characteristic peaks for γ-MnO_2 (JCPDS card no. 14-0644). Except for these characteristic peaks, no additional peaks could be observed, indicating the pure phase of MnO_2. The visible broad peaks and unsmooth basal of the diffraction pattern suggest that the material may possess a nano structure with some amorphous nature.

The particle size distribution profiles of nano MnO_2 are shown in Fig. 1b. Most of the nano MnO_2 particles have dia-

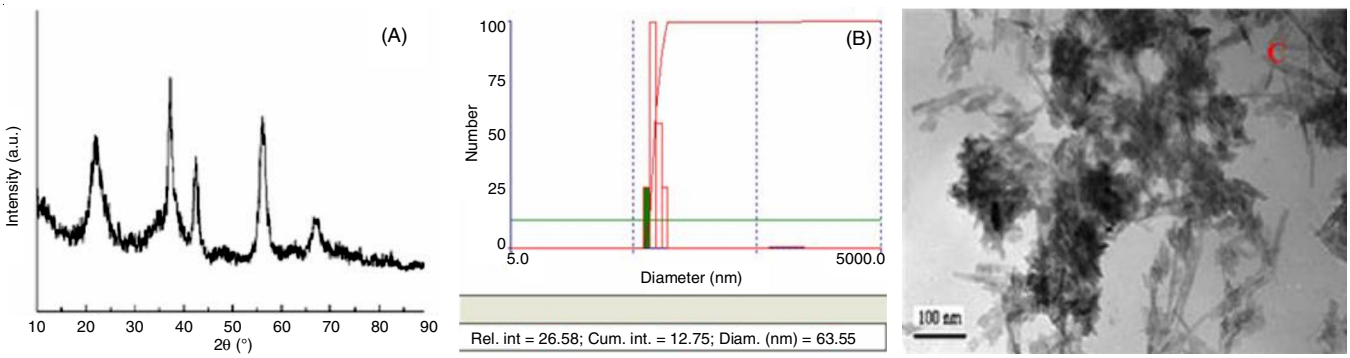

Fig. 1. (A) XRD pattern of nano MnO_2. (B) oarticle size distribution profile of nano MnO_2(C) TEM image of nano MnO_2

meters 63.55 nm. The particle size distribution profile observation has comparable results as that of XRD pattern and confirmed the nanosized dimension of the prepared composites. Fig. 1c shows the transmission electron microscope image of the MnO_2 sample. It was clear that the particles was composed of needle-like nano rods with a diameter ranging from several to about 10 nm and a length ranging from 10-100 nm.

Microstructural analysis: The main objective of the present work was the metallurgical improvement as it is the main parameter that can be significantly improved by means of nano MnO_2 incorporation. The macro structural characteristics of the prepared anode were evaluated by optical microscopy. Fig. 2a displays the morphological characteristics of bare Al-alloy anode while Fig. 2b shows that of nano MnO_2 integrate Al-alloy anode at low magnification. Fig. 3a displays the morphological structures of bare Al-alloy anode while Fig.3b that of the nano MnO_2 incorporated Al-Zn anode at low magnification and Fig. 3c and Fig. 3d show that of nano MnO_2 incorporated Al-Zn anode at higher magnifications. A reasonable distinct in the morphological structures of the two anodes were clearly visible during the analysis. The micrograph of the nano MnO_2 incorporated Al-Zn anode also had uniform grain size with slight segregation of MnO_2 distributed regularly through out the entire surface. No other concrete damages like localized void, intergranular crack and channel was observed. The smaller and uniform grain size could have significant impact on the galvanic characteristics of the anode. Moreover, in the present case, the whole area of Al-Zn anode was found relatively more defective than the nano MnO_2 incorporated Al-Zn anode as there were many voids and cracks found on the former. Anodes having defective morphology usually lead to localized corrosion resulting low galvanic efficiency [28].

Electrochemical evaluation of anode

OCP characteristics: OCP, a reliable parameter indicating the activation/passivation of anode and it defines as the stable open circuit potential without any electrical disturbance. Activation of Al anodes were generally demonstrated by varying of the OCP and pitting potential in the cathodic region. Fig. 4 displays the trend of OCP characteristics of the sacrificial anodes incorporated with varying amounts of MnO_2, in artificial sea water for a time period of 60 days. The initial OCP values of MnO_2 incorporated anodes were display in the range of-0.950 to -0.989 V and were to shifted to -0.947 to -0.981 V after 60 days of study. There were stable potential fluctuations only at the beginning and the potential value became gradually increased as the experimentation time of exposure continued. The equilibrium OCP at the beginning was due to the presence of quasi-stable Al_2O_3 layer [29]. However, as the period of time exposure increased, the Al_2O_3 film became unable to protect the substrate from further active disintegration due to cathodic breakdown and the Al_2O_3 layer hydrates [8]. Among the anodes,

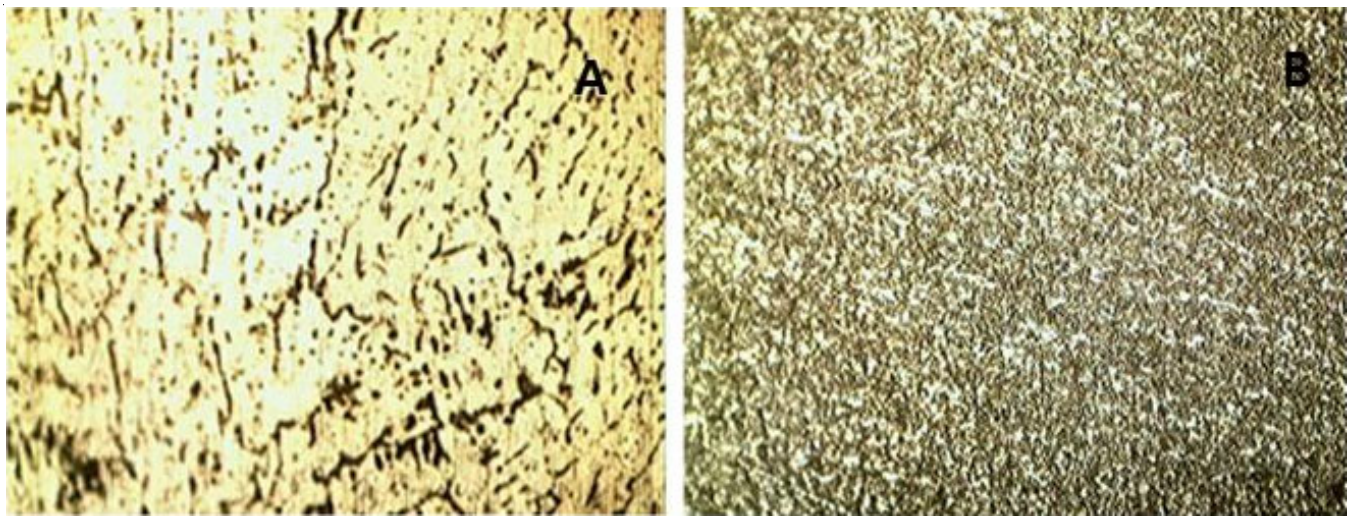

Fig. 2. Optical micrograph of (A) Al-Zn, (B) Al-Zn + MnO_2

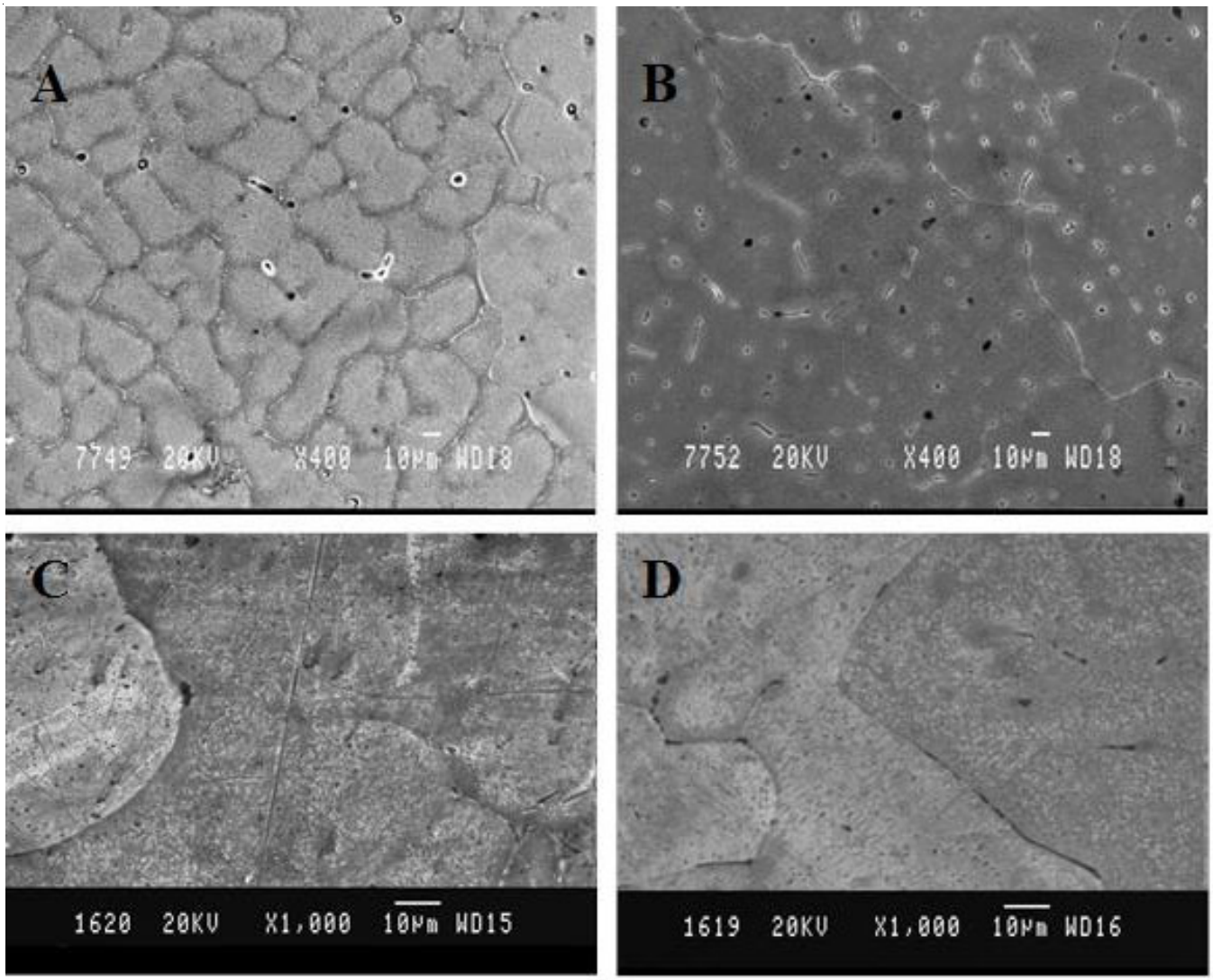

Fig. 3. SEM micrographs of (A) Al-Zn, (B) Al-Zn + MnO_2; (C) and (D) are at higher magnifications respectively

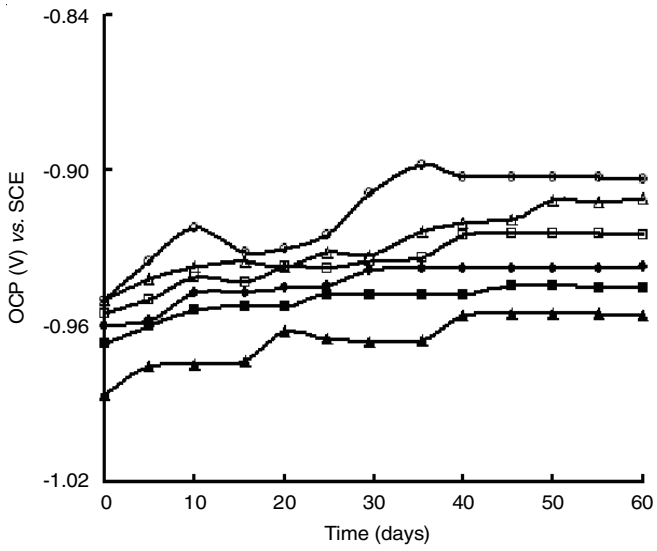

Fig. 4. OCP variation of Al-Zn anode with different amounts of MnO_2 incorporation for a period of 60 days (Cathode: Mild steel, electrolyte: 3 % NaCl) (○) 0%, (△) 0.05%, (□) 0.1%, (●) 0.2%, (▲) 0.5%, (■) 1%

0.5 % MnO_2 incorporated anode exhibited highest OCP shift; –0.042 V in the cathodic way as that of pure Al-Zn anode.

Self corrosion: The rate self-corrosion of the anodes was studied to calculate the non-columbic metal loss, since it was the major drawback of Al rich sacrificial anodes. Corrosion rate was evaluated by determining the anode mass that has been disintegrated purely due to ongoing galvanic reactions. Table-1 shows the rate of self corrosion of the anodes for two months of immersion in 3 % NaCl solution. The self-corrosion values of the pure Al-Zn anode was 10.952×10^{-6} g/cm^2/h and that of the nano MnO_2 incorporated anodes was found in the range of 10.952×10^{-6} to 7.19×10^{-6} g/cm$_2$/h. From various anodes under experimentation, 0.5 % nano MnO_2 incorporated anode displayed the lowest self-corrosion rate. An efficient sacrificial anode must have low self-corrosion value in order to avoid frequent anode replacement. The reduction in self-corrosion values of the nano MnO_2 incorporated Al-Zn anode could be due to the suppression of deterioration along grain boundaries due to enhanced grain depuration [9]. The lack of other metallurgical defects such as voids and creaks was also the reason for low self corrosion and high coulombic efficiency.

TABLE-1
METALLURGICAL AND GALVANIC PERFORMANCE OF THE NANO MnO_2 INCORPORATED Al-Zn ALLOY SACRIFICIAL ANODE

Wt. of MnO_2 (%)	OCP *vs.* SCE (V)	CCP *vs.* SCE (V)	Weight loss ($\mu g\ cm^{-2}\ h^{-1}$)	Long term efficiency (%)	Accelerated efficiency (%)	Micro hardness (VHN)
–	-0.930	-0.912	10.860	54.5	25.1	39 ± 1.4
0.05	-0.940	-0.923	08.215	60.1	28.4	43 ± 2.2
0.1	-0.945	-0.927	08.152	61.7	30.9	44 ± 1.8
0.2	-0.948	-0.930	07.861	63.0	32.7	47 ± 2.5
0.5	-0.970	-0.950	07.159	80.0	66.7	52 ± 1.8
1.0	-0.959	-0.943	07.299	75.0	59.5	52 ± 2.9

Long-term galvanic efficiency: The anode efficiency for a period of three months of immersion in 3% NaCl was studied with reference to accelerated electrochemical test. From Table-1, it was clear that the galvanic efficiency of bare Al anode was significantly lower than MnO_2 incorporated anode. Theoretically, lower galvanic efficiency of the anodes was due to the presence of impurities where deterioration occurs through a narrow spot in the grain boundaries [30]. In present case, 0.5% nano MnO_2 incorporated anode exhibited remarkably high efficiency, around 59%, revealing uniform anode dissolution. It was assumed that with the introduction of MnO_2 composite, the surface interface reactions were substantially reduced and the mechanical grain loss effectively suppressed, which synergistically enhanced the galvanic efficiency. All the anodes exhibited galvanic efficiency values in accordance with accelerated electrochemical test. The pure Al-Zn anode displayed efficiency of only 58%. On the other hand, Al-Zn+0.5% MnO_2 anode had substantially and relatively high efficiency as 70% during the accelerated tests. This revealed long-term uniform anode dissolution by the uniform presence of nano NiO in the interior mass of the anode, during the galvanic exposure. The galvanic efficiency of the anodes increased with increase in nano MnO_2 concentration up to 0.5%. A gradual increase in the amount of nano MnO_2 prevented the formation of passive oxide film on the anode surface. Further increase in the nano MnO_2 content in the Al-Zn matrix reduced the galvanic efficiency due to the increase in the barrier properties of the anode surface. Thus it became clear that keeping the optimum concentration of nano MnO_2 (0.5%) was critical to get high efficiency of the anode.

Electrochemical impedance characterization: The electrochemical impedance spectroscopy provides useful information to describe the active behaviour of complex corrosion system. Electrode impedance is a complex number and the impedance spectra are normally displayed in a Nyquist (complex plane) plot, where the imaginary part of impedance (-Z″) is plotted against real part (Z′). Fig. 5a shows the Nyquist plots of EIS data obtained for bare anode, while Fig. 5b shows the MnO_2 incorporated Al-Zn alloy sacrificial anode. From the impedance plots, it could be observed that bare anode had a wide arc in the high frequency region. A similar trend was observed in the case of nano MnO_2 incorporated Al-Zn anode also. However, the polarization resistance (R_p) values of nano MnO_2 incorporated Al-Zn was found to be lower than that of Al-Zn anode. The polarization resistance (R_p) was an indication of effective interaction between the oxide film and the substrate, which could lower the surface resistance. The lowering of surface resistance was requisite for an efficient sacrificial anode.

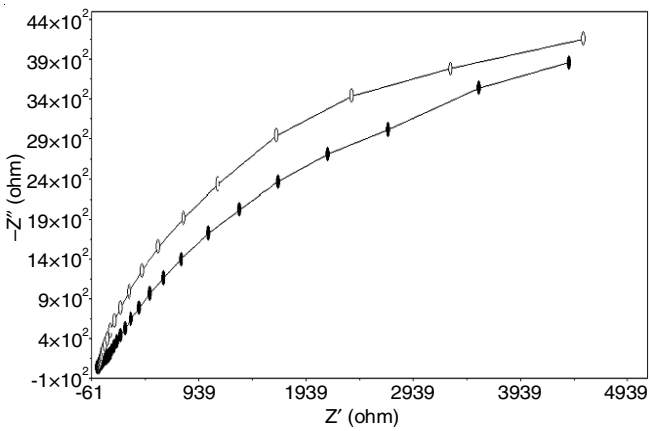

Fig. 5. Nyquist diagrams of Al-Zn anode incorporated with (O) Al-Zn, (●)Al-Zn + MnO_2 3 % NaCl solution in the frequency range of 1 MHz to 0.1 Hz with reference to OCP

The dominant and wide arc observed from the Nyquist plot of MnO_2 incorporated anode could be attributed to formation of thin alumina layer on the outer most surface of the anode. The impedance spectra also revealed that the incorporation of both bare anode and MnO_2 into Al-Zn anode led to destabilization of the weak layer of Al_2O_3 and the inner composite-aluminum layer as required for effective cathodic protection.

According to Bode plot (Fig. 6), obvious change in the Z modulus can be found as a result of the incorporation of nano MnO_2 into Al-Zn alloy anode. The Z modulus of nano MnO_2 incorporated Al-Zn anode exhibited lower value and the linear slope modulus gradually decreased compared to Al-Zn anode. Theoretically, lower Z modulus at lower frequency displays better sacrificial action of the anode. The phase angle plotted against logarithm of the frequency is also shown in Fig. 6. The appearance of an inductive loop at low frequencies could be attributed to the formation of an intermediate when the alloy undergoes active dissolution [31]. The inductive loop observed in the low frequency region could also be attributed to the slow relaxation process of hydrogen adsorption as well as aluminum dissolution in the form of Al^{3+} ions. The origin of inductive response of aluminum alloy revealed poor layer homogeneity, which could be due to the pore structure and possible adsorption relaxation process resulting in pitting corrosion [32,33]. In addition, the impedance spectrum revealed a phase angle close to 70º over a short range of frequencies for Al-Zn anode while MnO_2 incorporated Al-Zn anode shows a phase angle of only 50º. The lowering of phase angle values of nano MnO_2 incorporated Al-Zn anodes could be attributed to the effective destabilization of passive alumina layer on the anode surface.

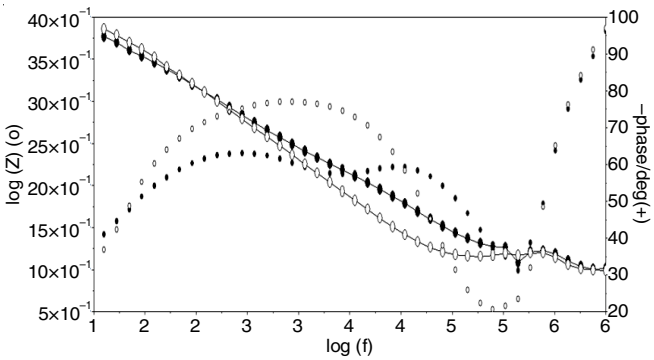

Fig. 6. Bode plots of Al-Zn anode incorporated with (○) Al-Zn , (●) Al-Zn + MnO_2

It is well known that a pure capacitive behaviour is plotted as the phase angles gradually increase and reaches to 90º [34,35]. The decrease in both R_p and phase angle values is a clear indication of effective interaction between the oxide film and the substrate that lowers surface resistance.

Dissolution rate of the anode with different solution flow rate: The effect of electrolyte velocity on dissolution rate of the anode in condensed media was a very well-known issue. The dissolution of the anode in condensed media involves at least three fundamental steps: (i) transport of the reactant to the anode surface; (ii) electron exchange resulting in metal loss; and (iii) transport of the corrosion products from the anode surface to the bulk solution.

Because the three steps occur in series, any one of them can control the rate of the overall process. Accordingly, it was necessary to take into account of both charge transfer and mass transfer phenomena when describing the dissolution of anode in marine environments. In other words, hydrodynamic factors play a key role in the kinetics of galvanic anode dissolution. Mass transfer and surface shear effects may have a profound effect on the rate of anode dissolution, either by modifying the rate of transport of chemical species to or from the surface or by shear-stripping protective films from the alloy/solution interface [36].

It can be seen from Fig. 7 that the dissolution rate of anode increases with increasing chloride concentration in agreement with significant negative shift in the pitting potential of anode. This may attributable to the increase in both anodic current output and solution conductivity. The increase in anodic current output at potentials where pure Al-Zn normally expected to be passive was due to the effective degradation of surface alumina layer. The insensitivity of rate of dissolution of anode at higher NaCl concentration (> 5%) was associated with decrease in the concentration of dissolved O_2 gas as a result of the salting out effect caused by NaCl [36]. It can also be seen that the dissolution rate of anode increases with the increasing flow rate of chloride medium. This may be attributed to the decrease in thick-ness of hydrodynamic boundary layer and diffusion layer across which dissolved oxygen diffuses to steel cathode according to the following equation [37] $J = K = D\,C_{O_2}/\delta$; where J = mole flux of oxygen, K = mass transfer coefficient, C_{O_2} = saturation solubility of O_2 in water, D = diffusivity of oxygen in chloride solution and δ = boundary layer thickness. Then

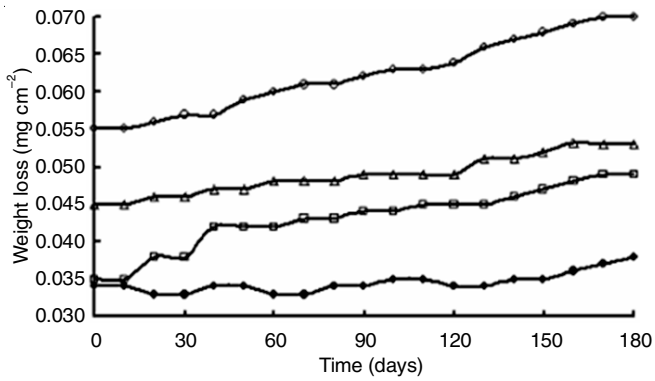

Fig. 7. Effect of electrolyte flow rate on dissolution of MnO_2 incorporated Al-Zn anode (●) 300 L h^{-1}, (□) 400 L h^{-1}, (△) 500 L h^{-1}, (○) 600 L h^{-1}

the passive alumina layer almost vanishes and the products of corrosion and protective films were continuously swept away from anode surface resulting effective anodic dissolution. The effective dissolution of the anode and remarkable negative shift in pitting potential value of the developed anode relative to pure Al-Zn anode itself manifests its anodic activation capacity in aggressive marine conditions.

Tolerance of anode in different aggressive media: The variation of anode potential, OCP and CCP as a function of time when the anodes were immersed in aggressive chloride environments are shown in Fig. 8. As the concentration of NaCl solution increases from 3 to 10% both OCP and CCP values shifted to more negative region compared to pure Al-Zn anode. In aggressive marine media, the cathodic reaction possible was hydrogen evolution either by dissociation of water molecules catalyzed by Al_2O_3 film or chemical attack by OH^- and water accordingly as:

$$2H_2O \longrightarrow H_3O^+ + OH^- \quad (1)$$

$$2H_3O^+ + e^- \longrightarrow H_2 + 2\,H_2O \quad (2)$$

$$Al + OH^- + H_2O \longrightarrow AlO_2^- + 3/2H_2 \quad (3)$$

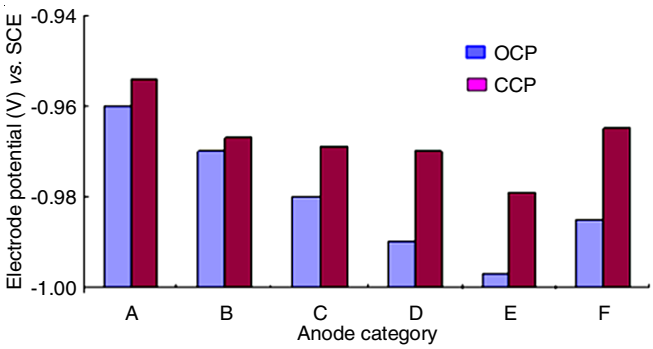

Fig. 8. OCP and CCP decay trend of Al-Zn alloy anode with different amounts of MnO_2 incorporation in 10% NaCl solution (A) 0%, (B) 0.05%, (C) 0.1%, (D) 0.2%, (E) 0.5%, (F) 1%

The released hydrogen react with anode surface to form substance such as AlH_3, AlH_2^+ and AlH^{2+}, which may shifts the potential to more negative region [38]. Moreover, hydration of the oxide film takes place as a consequence of local pH increase (alkalizing effect) at the oxide/solution interface by

hydrogen splitting away from water. The hydrated part of the oxide film was assumed to penetrate towards the metal/oxide interface. This resulted in the increase in ionic conductance inside this portion of the film and in an increased rate of electron transfer (tunnelling) through the remaining anhydrous part. Finally, hydrogen was being evolved at the bare metal at an anomalous yield due to a simultaneous and equivalent dissolution of the metal.

Morphological characterization during long-term immersion: Corrosion of aluminum alloys usually occurs as a result of two major electrochemical reactions involving the anodic area where metal dissolution occurs ($Al \rightarrow Al^{3+} + 3e^-$) and the cathodic areas where the reactions such as reduction of oxygen ($O_2 + 2H_2O + 4e^- \rightarrow 4OH^-$) occur. The representative corroded surfaces of nano NiO incorporated Al-Zn anode after different immersion time are shown in Fig. 9. No significant corrosion pits could be observed initially as also shown in Fig. 9a. Some pits with average size of 4 µm became distinguishable after 30 min immersion (Fig. 9b). This was probably due to the initiation of activation mechanism. Generally, aluminum activation in solutions containing aggressive ions can be initiated at active sites through pitting. Then the flaws site of anode surface, such as precipitates can further cause the initiation and propagation of the pitting. Hence the presence of small pits on the anode surface can act as corrosion nuclei and can be beneficial to the sacrificial action of the anode. The size of the pits was gradually increased without increase in pits number up to 1 h immersion (Fig. 9c). In this case no other precipitates were seen on the anode surface. Special features like mud-structured grain were developed on the anode surface after 10 h immersion (Fig. 9d). Generally mud structure on the anode surface can be explained by considering passivation on the anode as a dynamic process [39]. Moreover, precipitates of corrosion products were relatively small. This indicated that fine dispersoids were not active in localized corrosion processes. The corroding sites are most likely related to the cathodic intermetallic particles that have sufficient potential difference relative to the matrix, so that local anodic dissolution of the matrix starts in the boundary region adjacent to the particles [40].

Antifouling effect: Biological organisms present in the marine environments often have the potential to increase or decrease oxygen transport to the anode surface; consequently, these organisms have a critical role in affecting the performance of the anode. Electrostatic, van der Waals and Lewis acid base interactions govern adhesion of bacteria on solid surface. Both bacterial and solid surface properties like solid roughness and hydrophobicity govern the initial adhesion phase of bacteria on the surface. It has been documented that the composite incorporation in Al matrix has significant effect in resisting biofouling in marine environments. This synergistic action was probably due to the shifting of electronic absorption to higher wavelength region and formation of labile oxygen vacancies [41]. The number of cell colonies attached to pure Al-Zn anode was 2350 CFU cm^{-2}, while the presence of MnO_2 activators in the interior of Al-Zn anode remarkably reduces the colony formation, only 1500 CFU cm^{-2}. The significant reduction in bacterial reduction was probably due to the formation of hydroxyl radical and hydrogen peroxide during enhanced oxygen reduction reactions. This result lay strong emphasize on the potential scope of MnO_2 incorporated Al-Zn sacrificial for effective cathodic protection system especially in marine environments.

Conclusion

The incorporation of MnO_2 into aluminium alloy promoted active sacrificial dissolution of the anodes. The activation was manifested by shifting of the open circuit potential in the negative direction. The mechanical properties of the anodes were enhanced significantly by MnO_2 inclusion resulting significant reduction in non-columbic metal loss. The electrochemical characteristics of the anodes were enhanced due to effective

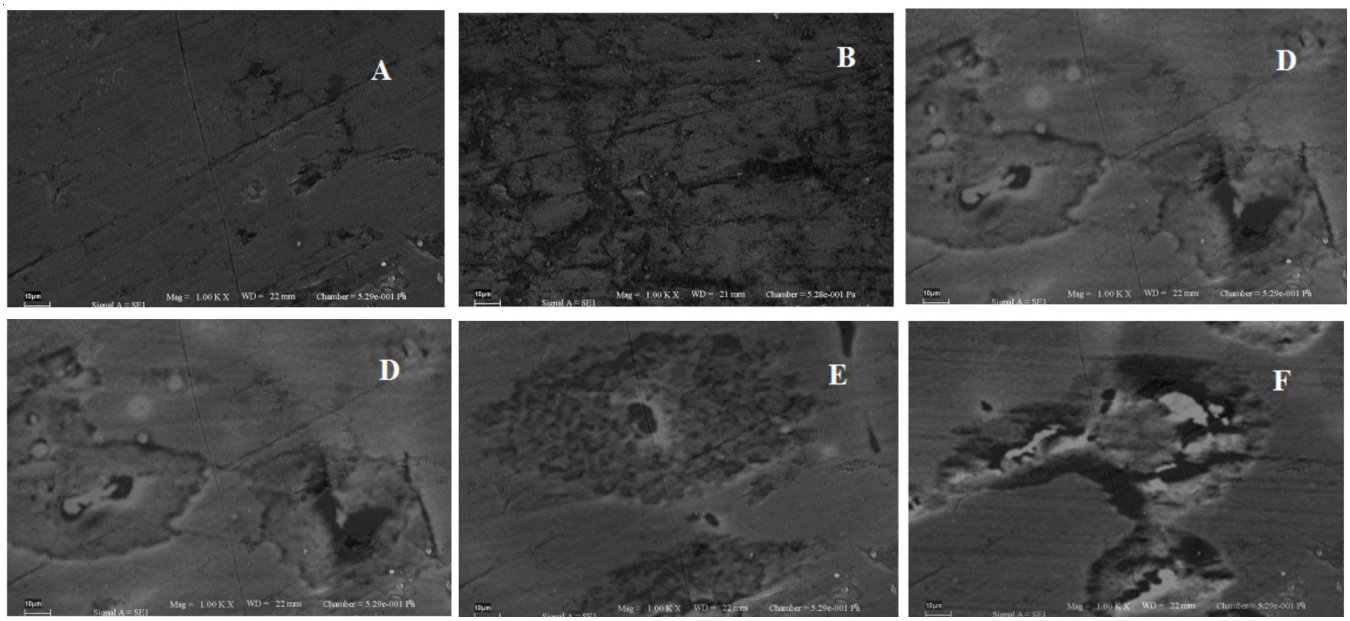

Fig. 9. SEM micrographs of Al-Zn anode incorporate with nano MnO_2 incorporated after immersed in 3% NaCl solution for (A) 10 min, (B) 30 min, (C) 1 h, (D) 10 h, (E) 3 days, and (F) 30 days

suppression of local macro/micro-cell action and mechanical loss. The EIS was applied in analysis of the activation and passivation of aluminium alloy anode, as it distinguish the elementary processes taking place at the anode. The galvanic efficiency of 83.4% was achieved by the active dissolution of MnO_2 into matrix. The activation mechanism was interpreted on the basis of autocatalytic dissolution-redeposition attack of activator on the anode surface. The fabricated anodes were consociated with further merits of cost effective, easy molding technique and endurance in aggressive chloride media.

CONFLICT OF INTEREST

The authors declare that there is no conflict of interests regarding the publication of this article.

REFERENCES

1. C. Gonzalez, J. Genesca, O. Alvarez and J.A. Juarez-Islas, *Metall. Mater. Trans., A Phys. Metall. Mater. Sci.*, **34**, 2991 (2003); https://doi.org/10.1007/s11661-003-0198-6
2. M. del Rosario Silva Campos, C. Blawert, N. Scharnag, M. Störmer and M.L. Zheludkevich, *Materials*, **15**, 1301 (2022); https://doi.org/10.3390/ma15041301
3. A. Barbucci, P.L. Cabot, G. Bruzzone and G. Cerisola, *J. Alloys Compd.*, **268**, 295 (1998); https://doi.org/10.1016/S0925-8388(97)00605-1
4. S.Z.E. Abedin and F. Endres, *J. Appl. Electrochem.*, **34**, 1071 (2004); https://doi.org/10.1023/B:JACH.0000042672.23588.df
5. D.O. Flamini, S.B. Saidman and J.B. Bessone, *Thin Solid Films*, **515**, 7880 (2007); https://doi.org/10.1016/j.tsf.2007.04.016
6. J.L. Ma, J.B. Wen and X.W. Lu, *Corros. Sci.*, **51**, 2115 (2009); https://doi.org/10.1016/j.corsci.2009.05.039
7. J.L. Ma and J. Wen, *J. Alloys Compd.*, **496**, 110 (2010); https://doi.org/10.1016/j.jallcom.2010.02.174
8. D.R. Salinas, S.G. Garcia and J.B. Bessone, *J. Appl. Electrochem.*, **29**, 1063 (1999); https://doi.org/10.1023/A:1003684219989
9. S.M.A. Shibli, B. Jabeera and R. Manu, *Mater. Lett.*, **61**, 3000 (2007); https://doi.org/10.1016/j.matlet.2006.10.062
10. Y. Zhan and G. Zhang, *Mater. Lett.*, **57**, 4583 (2003); https://doi.org/10.1016/S0167-577X(03)00365-3
11. G. Karunakaran, R. Suriyaprabha, V. Rajendran and N. Kannan, *IET Nanobiotechnol.*, **10**, 171 (2016); https://doi.org/10.1049/iet-nbt.2015.0007
12. P.M. Ashraf and S.M.A. Shibli, *Electrochem. Commun.*, **9**, 443 (2007); https://doi.org/10.1016/j.elecom.2006.09.010
13. P.M. Ashraf and L. Edwin, *J. Alloys Compd.*, **548**, 82 (2013); https://doi.org/10.1016/j.jallcom.2012.09.020
14. S.R. Archana, P.S. Arun, B.R. Sreelekshmi and S.M.A. Shibli, *Mater. Sci. Eng. B*, **261**, 114768 (2020); https://doi.org/10.1016/j.mseb.2020.114768
15. B. Balaraju, S. Kaleemulla and C. Krishnamoorthi, *J. Magn. Magn. Mater.*, **464**, 36 (2018); https://doi.org/10.1016/j.jmmm.2018.05.039
16. Y. Dong, J. Zhao, J.Y. Zhang, Y. Chen, X. Yang, W. Song, L. Wei and W. Li, *Chem. Eng. J.*, **388**, 124244 (2020); https://doi.org/10.1016/j.cej.2020.124244
17. K. Rajendra Prasad and N. Miura, *Electrochem. Commun.*, **6**, 1004 (2004); https://doi.org/10.1016/j.elecom.2004.07.017
18. K.M. Racik, K. Guruprasad, M. Mahendiran, J. Madhavan, T. Maiyalagan and M.V.A. Raj, *J. Mater. Sci.: Mater. Electr.*, **30**, 5222 (2019); https://doi.org/10.1007/s10854-019-00821-3
19. J. Liu, J. Jiang, M. Bosman and H.J. Fan, *J. Mater. Chem.*, **22**, 2419 (2012); https://doi.org/10.1039/C1JM14804D
20. S.G. Hwang, S.H. Ryu, S.R. Yun, J.M. Ko, K.M. Kim and K.S. Ryu, *Mater. Chem. Phys.*, **130**, 507 (2011); https://doi.org/10.1016/j.matchemphys.2011.07.022
21. H. Kim and B.N. Popov, *J. Electrochem. Soc.*, **150**, 56 (2003); https://doi.org/10.1149/1.1541675
22. P.C. Maity, P.N. Chakraborty and S.C. Panigrahi, *Mater. Lett.*, **20**, 93 (1994); https://doi.org/10.1016/0167-577X(94)90068-X
23. A.A. Hamid, S.C. Jain, P.K. Ghosh and S. Ray, *Metall. Mater. Trans., A Phys. Metall. Mater. Sci.*, **36**, 2211 (2005); https://doi.org/10.1007/s11661-005-0340-8
24. A.A. Hamid, P.K. Ghosh, J.C. Jain and S. Ray, *Wear*, **260**, 368 (2006); https://doi.org/10.1016/j.wear.2005.02.120
25. C.J. Clarke, G.J. Browning and S.W. Donne, *Electrochim. Acta*, **51**, 5773 (2006); https://doi.org/10.1016/j.electacta.2006.03.013
26. D.K. Walanda, G.A. Lawrance and S.W. Donne, *J. Power Sources*, **139**, 325 (2005); https://doi.org/10.1016/j.jpowsour.2004.06.062
27. D. Wang, Z.Y. Ma and Z.M. Gao, *Mater. Chem. Phys.*, **117**, 228 (2009); https://doi.org/10.1016/j.matchemphys.2009.05.048
28. S.M.A. Shibli, S.R. Archana and P. Muhamed Ashraf, *Corros. Sci.*, **50**, 2232 (2008); https://doi.org/10.1016/j.corsci.2008.06.017
29. S.M.A. Shibli and K.K. Binoj, *J. Appl. Electrochem.*, **39**, 159 (2009); https://doi.org/10.1007/s10800-008-9659-3
30. S.M.A. Shibli, V.S. Dilimon and V.S. Saji, *J. Solid State Electrochem.*, **11**, 201 (2006); https://doi.org/10.1007/s10008-005-0088-5
31. S.M.A. Shibli and S. George, *Appl. Surf. Sci.*, **253**, 7510 (2007); https://doi.org/10.1016/j.apsusc.2007.03.052
32. J. He, J. Wen and X. Li, *Corros. Sci.*, **53**, 1948 (2011); https://doi.org/10.1016/j.corsci.2011.02.016
33. A. Venugopal and V.S. Raja, *Corros. Sci.*, **39**, 2053 (1997); https://doi.org/10.1016/S0010-938X(97)00082-6
34. J.B. Bessone, D.R. Salinas, C.E. Mayer, M. Ebert and W.J. Lorenz, *Electrochim. Acta*, **37**, 2283 (1992); https://doi.org/10.1016/0013-4686(92)85124-4
35. L. Bai and B.E. Conway, *Electrochim. Acta*, **38**, 1803 (1993); https://doi.org/10.1016/0013-4686(93)80302-G
36. H. Baorong, Z. Jinglei, L. Yanxu and Y. Fangying, *Mater. Corros.*, **52**, 219 (2001); https://doi.org/10.1002/1521-4176(200103)52:3<219::AID-MACO219>3.0.CO;2-W
37. A.S. Yaro, H. Aljendeel and A.A. Khadom, *Desalination*, **270**, 193 (2011); https://doi.org/10.1016/j.desal.2010.11.045
38. S. Gudic, J. Radosevic, I. Smoljko and M. Kliskic, *Electrochim. Acta*, **50**, 5624 (2005); https://doi.org/10.1016/j.electacta.2005.03.041
39. K. Sasaki and G.T. Burstein, *Corros. Sci.*, **38**, 2111 (1996); https://doi.org/10.1016/S0010-938X(96)00066-2
40. J.L. Ma, J.B. Wen and X.W. Lu, *Corros. Prot.*, **30**, 373 (2009).
41. B. Li and B.E. Logan, *Colloids Surf. B Biointerfaces*, **41**, 153 (2005); https://doi.org/10.1016/j.colsurfb.2004.12.001